Applied Physics Letters

Terahertz metamaterial perfect absorber with continuously tunable air spacer layer

Cite as: Appl. Phys. Lett. **113**, 061113 (2018); https://doi.org/10.1063/1.5041282
Submitted: 23 May 2018 . Accepted: 25 July 2018 . Published Online: 10 August 2018

Jacob Schalch, Guangwu Duan, Xiaoguang Zhao, Xin Zhang, and Richard D. Averitt

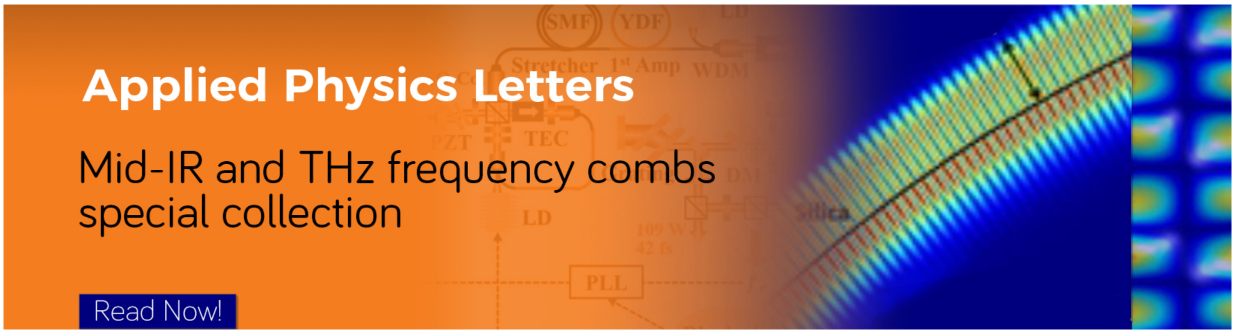

Appl. Phys. Lett. **113**, 061113 (2018); https://doi.org/10.1063/1.5041282 **113**, 061113

APPLIED PHYSICS LETTERS **113**, 061113 (2018)

Terahertz metamaterial perfect absorber with continuously tunable air spacer layer

Jacob Schalch,[1] Guangwu Duan,[2] Xiaoguang Zhao,[2] Xin Zhang,[2,a)] and Richard D. Averitt[1,a)]
[1]*Department of Physics, University of California, San Diego, La Jolla, California 92093, USA*
[2]*Department of Mechanical Engineering, Boston University, Boston, Massachusetts 02215, USA*

(Received 23 May 2018; accepted 25 July 2018; published online 10 August 2018)

We present a comprehensive investigation of a continuously tunable metamaterial perfect absorber operating at terahertz frequencies. In particular, we investigate a three-layer absorber structure consisting of a layer of split ring resonators and a metallic ground plane, with a central layer consisting of a mechanically tunable air-spaced layer. The absorber was characterized using terahertz time-domain spectroscopy in reflection (at normal incidence) as a function of spacer thickness from 0 to 1000 μm. Our experimental measurements reveal the detailed evolution of the absorption bands as a function of spacing, in excellent agreement with analysis using interference theory and simulation. Our Fabry-Pérot-like structure provides an avenue for achieving massive tunability in metamaterial absorber devices. *Published by AIP Publishing.* https://doi.org/10.1063/1.5041282

Materials that exhibit near perfect absorption of electromagnetic (EM) waves are important for a wide variety of photonic applications including energy harvesting,[1] communications,[2] and chemical and biological sensing,[3,4] among others. Metamaterials (MMs) are artificial materials with a periodic subwavelength structure designed to exhibit a tailored response[5–7] and have played a crucial role in the realization of perfect absorbers. Metamaterial perfect absorbers (MPAs) are a class of MMs designed to achieve near unity absorption by minimizing the reflectivity through tuning the effective permittivity and permeability to match the impedance of free space. MPAs typically consist of three layers, a metamaterial layer, a dielectric spacer layer, and a metallic ground plane.[8,9] With a judicious choice of geometrical parameters and constituent materials, MPAs can display a number of unique absorption characteristics such as broad or narrow band absorption,[10,11] insensitivity to polarization and angle of incidence,[12,13] multiple absorption bands,[14] and tunability.[15–17] In addition, MPAs are optically thin and highly sensitive to the local dielectric environment, making such MMs especially well-suited for applications such as chemical sensing and biological detection.[18,19] MPAs which operate in the terahertz (THz) regime are of particular interest due, in part, to the novel application space afforded by this spectral range.

While MPAs are generally used in the thin spacer layer limit, it is important to note that a rich development of absorption resonances occurs with the increasing spacer layer thickness,[20] providing a potential route to tune the absorption with high precision. However, MPAs usually operate at distinct dielectric spacer layer thicknesses, limiting the tunability and making a detailed comparison with theory difficult.

We have overcome this limitation by creating a three-layer MPA operating at the THz frequencies ranging from ~0.1 to 2.0 THz. Our Fabry-Pérot-like device has two components: a gold ground plane and a MM layer consisting of split ring resonators (SRRs) on a thin silicon nitride (SiN_x) membrane. The two layers are separated with a central layer of air with a mechanically tunable thickness ranging from 0 to 1000 μm. Using a photo-conductive terahertz time domain spectrometer[21] (THz-TDS), we have performed detailed measurements of the electromagnetic response as a function of spacer layer thickness. The results are compared with interference theory based simulations that, in conjunction with the analytical results, provide a comprehensive description of our tunable MPA.

The variable air spacer MPA (VAS-MPA) consists of three components: a gold-coated wafer as the metallic ground plane, a stepper motor linear translation stage, and a free-standing MM layer (Fig. 1). The ground plane is a silicon wafer coated with a 200 nm thick gold layer, held in a holder at a fixed location. A free standing SRR/SiNx layer is held parallel to the ground plane and attached to a stepper motor translation stage which translates the MM layer to control the air spacer layer thickness, which can be adjusted to arbitrary thicknesses with a precision of 0.7 μm. The

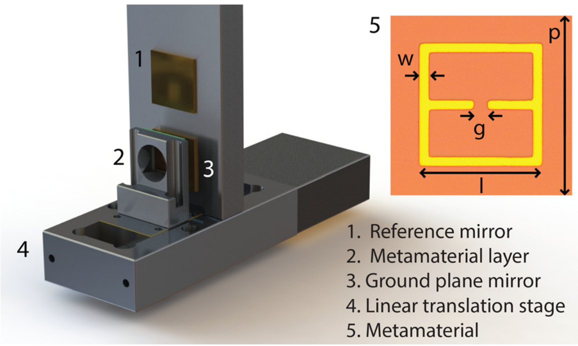

FIG. 1. Schematic of VAS-MPA. The SRR/SiN_x layer is parallel to the ground plane mirror and can be translated with high precision to create a spacer of arbitrary thickness. (Inset) A microscopy image of a single MM unit cell, where p = 120 μm, l = 110 μm, w = 5 μm, and g = 8 μm.

[a)] Authors to whom correspondence should be addressed: xinz@bu.edu and raveritt@ucsd.edu

free-standing MM layer was fabricated using micromachining techniques, starting with a double-sided silicon wafer coated with 400 nm thick SiN_x thin films. Photolithography and e-beam evaporation were utilized to fabricate the 200 nm thick gold SRRs on top of the substrate. Subsequently, the SiN_x thin film on the backside was patterned into a 10×10 mm window using photolithography followed by reactive ion etching. Finally, KOH wet etching was employed to completely remove the bulk silicon in the window region, leaving only the top SiN_x thin film with patterned SRRs.

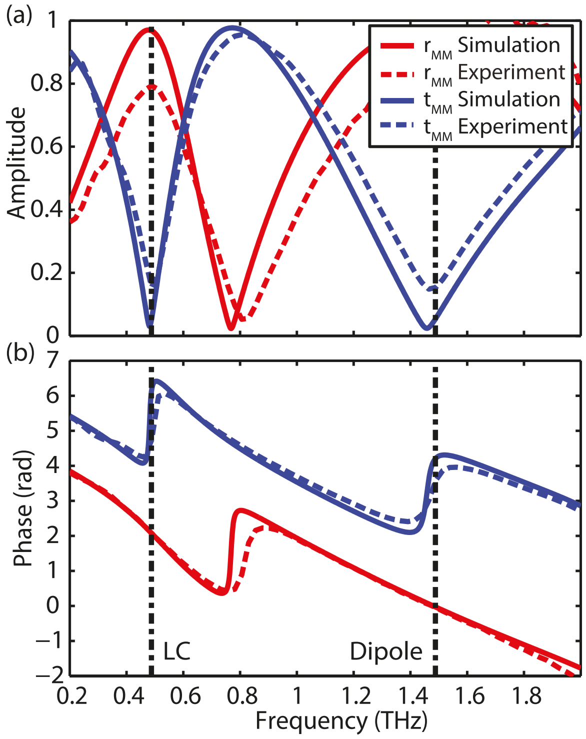

FIG. 2. The magnitude (a) and phase (b) of the transmission (blue) and reflection (red) coefficients for the isolated MM layer (i.e., in the absence of a ground plane). The dashed and solid lines correspond to the experimental measurement and numerical simulation results, respectively. The LC resonance (0.5 THz) and dipole resonance (1.5 THz) frequencies are marked with vertical dashed lines, corresponding to minima in transmission and maxima in reflection.

We utilize a home-built dual-mode THz-TDS system to measure the complex reflection and transmission coefficients of the isolated SRR/SiNx and VAS-MPA.[22] A titanium sapphire laser generates 800 nm, 20fs pulses at a repetition rate of 80 MHz, which is used to generate and detect the THz pulses using photoconductive antennas. The THz pulses impinge on the sample at normal incidence, and both transmission and reflection can be measured. For the transmission measurements of the isolated SRR/SiN_x layer, the transmitted pulse is compared with a reference pulse transmitted though air. For the reflection measurements of both the SRR/SiN_x layer and the VAS-MPA, the reflected pulse is compared with a reference pulse which is nearly perfectly reflected by a gold-coated silicon substrate. The time domain sample and reference pulses are Fourier transformed to obtain the frequency domain transmission and reflection spectra.

In order to characterize the evolution of the absorption spectrum of the VAS-MPA with the spacer layer thickness, we first measure the electromagnetic response of the isolated SRR/SiN_x layer. Figure 2 shows the complex reflection (r_{MM}) and transmission (t_{MM}) coefficients (amplitude and phase) of the SRR/SiN_x layer. The two lowest frequency resonant modes of the isolated SRR/SiN_x layer appear as minima in the transmission and maxima in the reflection. The fundamental inductor-capacitor (LC) resonance is at 0.5 THz, and the dipole resonance is at 1.5 THz. These results are verified by replicating the experiment numerically using the finite element method frequency domain (FEMFD) solver CST Microwave Studio 2016 (solid lines). For the simulations, we construct a unit cell geometry of the SRR/SiNx where gold is modeled as a lossy metal with a conductivity of 4.56×10^7 S/m and SiN_x is modeled as a lossy dielectric with a relative permittivity of $\varepsilon = 7.6(1 + 0.0053i)$.[23] Periodic boundary conditions are employed with a time domain plane wave pulse at normal incidence in order to retrieve the complex scattering parameters $S_{11} = r_{MM}$ and $S_{21} = S_{12} = t_{MM}$. The simulation results are plotted in Fig. 2, revealing excellent agreement with the experiment. These results can be used in conjunction with interference theory to model the absorption of the VAS-MPA as a function of the air spacer thickness.

The overall reflection can be accurately calculated as the superposition of multiple reflections[24]

$$r = r_{MM} - \frac{t_{MM}^2}{r_{MM} + e^{-i2\beta}}, \tag{1}$$

where r is the total reflection, $\beta = nkd$ is the one-way phase delay across the spacer, $n = 1$ is the refractive index of the spacer, k is the wave number in vacuum, and d is the spacer layer thickness. r_{MM} and t_{MM} are the complex reflection and transmission coefficients of the isolated SRR/SiN_x layer as presented in Fig. 2. Due to the presence of the metallic ground plane, the transmission channel of the absorber is entirely suppressed and the absorption can be calculated as $A = 1 - |r|^2$. Furthermore, this equation can be optimized and inverted in order to derive the spacer thickness that yields the maximum absorption at a given frequency[25]

$$d_m = -\frac{\theta}{2k} + \frac{m\pi}{k}. \tag{2}$$

In Eq. (2), θ is the phase of r_{MM} and m is an integer. This expression shows that, at a given frequency, multiple absorption maxima arise, associated with phase accumulations within the spacer layer which are integer multiples of 2π as in a traditional Fabry-Pérot cavity. A detailed derivation of a generalized version of Eq. (2) is presented in Ref. 20. The derivation is based on setting $dr/dd = 0$ in order to find spacer thicknesses which yield minima in reflection for a given frequency. Remarkably, this derivation demonstrates that the value of t_{MM} does not contribute to determining the values of d_m [see Eqs. (6)–(9) in Ref. 20]. We emphasize, however, that for determining frequencies and spacer thicknesses which yield perfect absorption, t_{MM} is relevant.

Figure 3(a) shows a color map of the measured THz-TDS absorption spectra of the VAS-MPA in reflection at normal incidence for different values of air spacer thickness

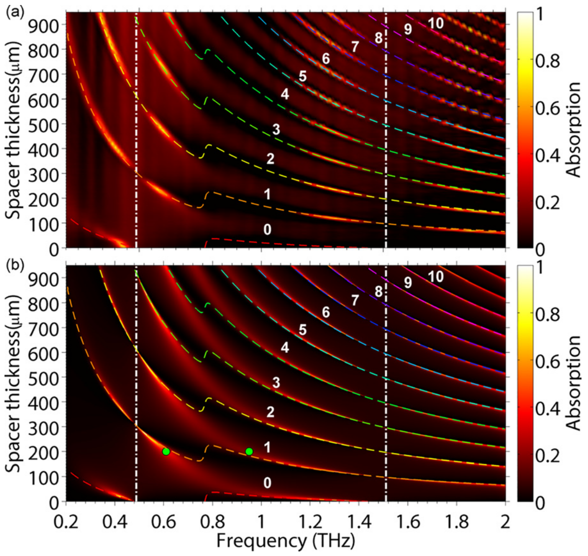

FIG. 3. Absorption spectra as a function of spacer layer thickness from (a) experimental THz-TDS reflection measurements and (b) interference theory. The LC and dipole resonance frequencies of the isolated MM layer (i.e., see Fig. 2) are marked with vertical dashed white lines, where absorption is strongly suppressed due to the large reflection from the SRR/SiNx. The *m*-curves and their associated value of *m* are marked with colored dashed lines. The green dots refer to the discussion associated with Fig. 5.

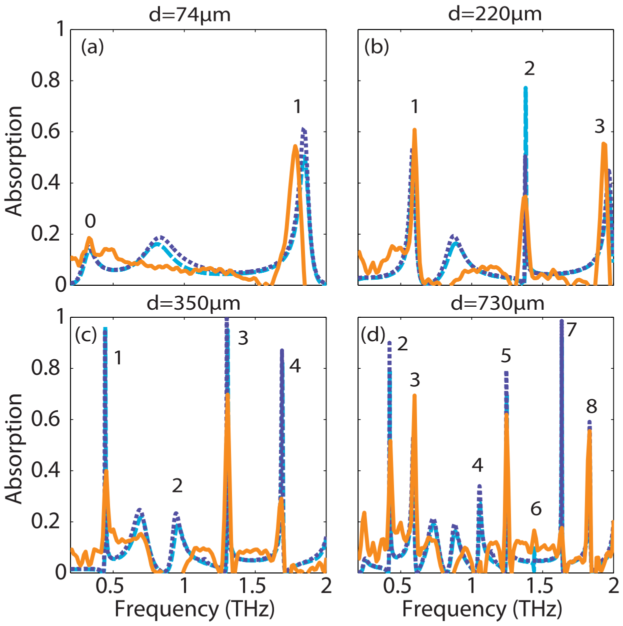

FIG. 4. Absorption spectra at several spacer layer thicknesses from interference theory calculations (dashed blue lines), experiments (solid orange lines), and FEMFD simulations (dotted purple lines). The value of the corresponding *m*-curve is noted for each peak.

d with a constant background subtracted to account for imperfect referencing. We start with a separation of one millimeter between the SRR/SiN$_x$ layer and the ground plane, measure the absorption spectrum, and then sequentially repeat the measurement, with the SRR/SiN$_x$ layer translated closer to the ground plane with each subsequent measurement, until the two are in direct contact. The decrement of spacer layer thickness *d* between measurements is 15 μm for $1000\,\mu\text{m} > d > 500\,\mu\text{m}$ and 5 μm for $500\,\mu\text{m} > d > 0\,\mu\text{m}$. To validate this result, Eq. (1) is used in conjunction with the simulated reflection and transmission of the SRR/SiN$_x$ layer to calculate the complex absorption of the VAS-MPA as a function of air spacer thickness *d* between 0 and 1 mm [Fig. 3(b)]. In Figs. 3(a) and 3(b), the LC and dipole resonant frequencies of the isolated SRR/SiN$_x$ layer are indicated with vertical dashed lines, around which absorption is suppressed due to the strong reflection and weak transmission at the SRR/SiN$_x$ layer. In the limit of zero spacer thickness, the absorption bands approach the LC and dipole resonance frequencies of the SRR/SiN$_x$ layer. As the air spacer thickness increases from zero, there is a dramatic redshift in both absorption bands, and additional bands emerge at higher frequencies. The emergence of these bands can be understood as a result of the phase delay within the spacer layer approaching integer multiples of 2π. Using Eq. (2), we can identify the air spacer thicknesses, that result in an absorption band. The result is a series of *m*-curves, shown with colored dashed lines in Figs. 3(a) and 3(b). Each is associated with a different integer value of *m* (shown) and thus $2\pi m$ phase accumulations within the spacer layer. The *m*-curves show excellent agreement with the analytical and experimental results.

Figure 4 compares the analytical [i.e., Eq. (1)] (dashed blue lines), experimental (orange lines), and FEMFD simulated (dotted purple lines) absorption spectra for several choices of spacer layer thicknesses. Each absorption band is labeled with the value of its corresponding *m*-curve (determined by examining the relevant horizontal cross-sections of Fig. 3). When $d = 74\,\mu m < \lambda/4$ [Fig. 4(a)], the spacer layer thickness and thus the entire unit cell are of subwavelengths corresponding to the metamaterial regime. The absorption bands associated with the 0th and 1st *m*-curve are visible. As the spacer layer thickness increases, absorption peaks associated with larger values of *m* begin to emerge. In this regime, very good agreement between the simulation, experimental, and interference theory results is apparent for each of the absorption bands. At $d = 730\,\mu$m [Fig. 4(d)], absorption peaks associated with *m*-curves 1 through 8 are all visible. The absorption peak amplitude is largest when the spacer layer is optimized for complete destructive interference of the reflected light for a specific frequency, but this condition is highly sensitive to the spacer thickness *d*; so, many of the peaks are well below unity absorption. For all spacer thicknesses, all three results (interference theory, FEMFD simulations, and experiment) show very good agreement. The experimental results show consistently smaller absorption amplitudes, not only due in part to imperfect referencing but also owing to the limited frequency resolution, which is evident for the narrowest absorption bands in particular. The other striking discrepancy between simulation, experiment, and interference theory occurs in the vicinity of 0.75 THz. Both the interference theory and the simulations show peaks which are more prominent relative to the experimental data. These peaks lie in a region where the phase of the reflection θ in Eq. (2) rapidly increases by $\sim\pi$, and the *m*-curves all increase by $\pi/2k$ accordingly. As such, interference theory is sensitive to any discrepancy in the input parameters, in particular those related to losses in SiN$_x$ and Au. As a result, peaks occur without any clear correspondence to one of the *m*-curves.

We have also investigated the dependence of the absorption peak linewidth. In Fig. 5, the Q-factor of the absorption peaks is obtained from the interference theory result and plotted as a function of spacer layer thickness d for a number of different m-curves, with each value of m indicated with a different color (as shown by the dashed lines in Fig. 3). We define the quality factor as $Q = f_a/\Delta f_a$, where f_a is the frequency of the absorption maxima and Δf_a is the full width at half maximum of the resonance, although it should be noted that many of the absorption peaks, particularly at larger values of d, are highly asymmetric. Likewise, note that the frequency of the absorption bands for a given value of m is inversely related to the spacer thickness d (see Fig. 3).

For absorption bands along each m-curve, a similar pattern emerges. It is therefore instructive to examine the Q-factor associated with $m = 1$ (orange dots) in detail, as this description can be generalized to all other values of m. The $m = 1$ curve first appears at $d = 70\,\mu$m and $Q = 15$ in Fig. 5, corresponding to the band emerging at 2 THz which is marked with an orange dashed line in Fig. 3. As d increases, the Q-factor reaches a maximum value of $Q = 115$ at $d = 95\,\mu$m. This corresponds to the m-curve crossing f_{dipole}. The Q-factor then decreases and vanishes as the absorption bands become indeterminate, corresponding to the previously mentioned jump in the m-curves. The band reemerges at $d = 200\,\mu$m and $Q = 9$. A similar behavior follows as a function of increasing d; the Q-factor first increases to a maximum of $Q = 99$ at $d = 296\,\mu$m (this time corresponding to the m-curve crossing f_{LC}), and then decreases and vanishes.

The m-curves are multi-valued as a function of d due to the previously discussed jump in the m-curves at ~0.75 THz. As a result, multiple Q factor values can occur for a single value of d and m. In the case of $m = 1$, at $d = 200\,\mu$m, both branches of the m-curve have the same value of Q (see the black square in Fig. 5), but these absorption bands are distinct and occur at different frequencies [see the green dots in Fig. 3(b)]. For all m-curves, there is generally a low-Q branch associated with lower frequencies and larger values of d and conversely a high-Q, high-frequency, low-d branch. Overall, the Q-factor increases with the values of m, reaching Q factors in excess of 400 for $m = 7$–10. We note that when the peaks become this narrow, the spectral resolution limits the magnitude of Q which can be resolved, given the spectral resolution of the simulation upon which the interference theory result is based. This constitutes a Q factor far larger than that of comparable THz MM absorbers although in this regime, the spacer layer thickness d is no longer of subwavelength.

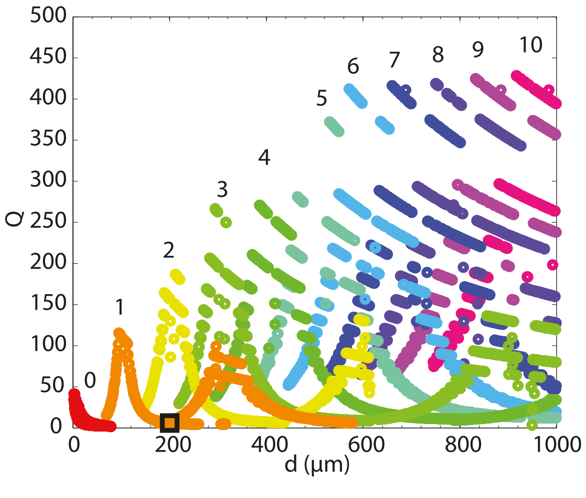

FIG. 5. Q factor of absorption peaks as a function of spacer layer thickness d for values of m between 0 and 10 as determined from interference theory [using Eq. (1)]. Each color corresponds to a different value of m (see Fig. 3). The black box highlights a region where more than one absorption can occur for a given value of m and d—see the green dots in Fig. 3 corresponding to this highlighted region.

We have experimentally realized a metamaterial-dielectric-metal absorber with a broadly tunable air dielectric layer. It has been demonstrated that the characteristics of the VAS-MPA can be accurately predicted using the interference theory of perfect absorbers, and we have comprehensively experimentally verified the evolution of the absorption bands of the absorber as a function of dielectric spacer layer thickness with THz-TDS. These measurements exhibited a high degree of agreement with both numerical simulations and analytical predictions. We characterized the observed absorption bands in relation to the m-curves predicted by interference theory. Finally, we examined the role of the spacer thickness in the absorption peak Q-factor, finding extremely large values in excess of $Q = 400$ for large spacer thicknesses and large values of m.

Our approach realizes an absorber device that, with relatively modest tuning of physical parameters, is capable of achieving a plethora of absorption characteristics: broad or narrow absorption bands, few or several absorption bands within the 0–2 THz regime, continuous frequency tunability, and continuous tuning of the absorption peak amplitude. While the practicality of this device is limited by the bulky translation stage, a micromechanically actuated analogue of the VAS-MPA could achieve a similar degree of tunability in a far smaller form factor. Likewise, it should be noted that all the results and analysis herein depend on the optical path length of the dielectric spacer layer, and thus, similar results can be achieved by modulating the refractive index of the dielectric layer rather than (or in addition to) its thickness d, which opens further possibilities for realization of practical devices. More generally, our results inform the design of metamaterial absorber devices where a high sensitivity to the dielectric environment, a wide degree of tunability, or a variable number absorption bands is desirable.

We acknowledge support from the National Science Foundation (NSF) (No. ECCS-1309835) and the Army Research Office (ARO) (NO. W911NF-16-1-0361). We thank the Boston University Photonics Center for technical support.

[1] T. K. Todorov, K. B. Reuter, and D. B. Mitzi, "High-efficiency solar cell with earth-abundant liquid-processed absorber," Adv. Mater. **22**, E156 (2010).

[2] Z. Sun, A. Martinez, and F. Wang, "Optical modulators with 2D layered materials," Nat. Photonics **10**, 227 (2016).

[3] Y. Hui and M. Rinaldi, "Fast and high resolution thermal detector based on an aluminum nitride piezoelectric microelectromechanical resonator with an integrated suspended heat absorbing element," Appl. Phys. Lett. **102**, 093501 (2013).

[4] N. Liu, M. Mesch, T. Weiss, M. Hentschel, and H. Giessen, "Infrared perfect absorber and its application as plasmonic sensor," Nano Lett. **10**, 2342–2348 (2010).

[5] D. R. Smith, W. J. Padilla, D. C. Vier, S. C. Nemat-Nasser, and S. Schultz, "Composite medium with simultaneously negative permeability and permittivity," Phys. Rev. Lett. **84**, 4184 (2000).

[6] D. R. Smith, J. B. Pendry, and M. C. K. Wiltshire, "Metamaterials and negative refractive index," Science **305**, 788–792 (2004).

[7] X. Zhao, K. Fan, J. Zhang, G. R. Keiser, G. Duan, R. D. Averitt, and X. Zhang, "Voltage-tunable dual-layer terahertz metamaterials," Microsyst. Nanoeng. **2**, 16025 (2016).

[8] E. F. C. Driessen and M. J. A. de Dood, "The perfect absorber," Appl. Phys. Lett. **94**, 171109 (2009).

[9] C. M. Watts, X. Liu, and W. J. Padilla, "Metamaterial electromagnetic wave absorbers," Adv. Mater. **24**, OP98–OP120 (2012).

[10] S. Gu, B. Su, and X. Zhao, "Planar isotropic broadband metamaterial absorber," J. Appl. Phys. **114**, 163702 (2013).

[11] A. A. Basharin, V. Chuguevsky, N. Volsky, M. Kafesaki, and E. N. Economou, "Extremely high Q-factor metamaterials due to anapole excitation," Phys. Rev. B **95**, 035104 (2017).

[12] D. Lim, D. Lee, and S. Lim, "Angle- and polarization-insensitive metamaterial absorber using via array," Sci. Rep. **6**, 39686 (2016).

[13] M. Wu, X. Zhao, J. Zhang, J. Schalch, G. Duan, K. Cremin, R. D. Averitt, and X. Zhang, "A three-dimensional all-metal terahertz metamaterial perfect absorber," Appl. Phys. Lett. **111**, 051101 (2017).

[14] J. W. Park, P. V. Tuong, J. Y. Rhee, K. W. Kim, W. H. Jang, E. H. Choi, L. Y. Chen, and Y. P. Lee, "Multi-band metamaterial absorber based on the arrangement of donut-type resonators," Opt. Express **21**, 9691–9702 (2013).

[15] J. Zhang, G. Wang, B. Zhang, T. He, Y. He, and J. Shen, "Photo-excited broadband tunable terahertz metamaterial absorber," Opt. Mater. **54**, 32–36 (2016).

[16] F. Hu, N. Xu, W. Wang, Y. Wang, W. Zhang, J. Han, and W. Zhang, "A dynamically tunable terahertz metamaterial absorber based on an electrostatic MEMS actuator and electrical dipole resonator array," J. Micromech. Microeng. **26**, 025006 (2016).

[17] M. Liu, M. Susli, D. Silva, G. Putrino, H. Kala, S. Fan, M. Cole, L. Faraone, V. P. Wallace, W. J. Padilla, D. A. Powell, I. V. Shadrivov, and M. Martyniuk, "Ultrathin tunable terahertz absorber based on MEMS-driven metamaterial," Microsyst. Nanoeng. **3**, 17033 (2017).

[18] L. Cong, S. Tan, R. Yahiaoui, F. Yan, W. Zhang, and R. Singh, "Experimental demonstration of ultrasensitive sensing with terahertz metamaterial absorbers: A comparison with the metasurfaces," Appl. Phys. Lett. **106**, 031107 (2015).

[19] A. Ishikawa and T. Tanaka, "Metamaterial absorbers for infrared detection of molecular self-assembled monolayers," Sci. Rep. **5**, 12570 (2015).

[20] G. Duan, J. Schalch, X. Zhao, J. Zhang, R. D. Averitt, and X. Zhang, "Analysis of the thickness dependence of metamaterial absorbers at terahertz frequencies," Opt. Express **26**, 2242–2251 (2018).

[21] M. Walther, G. S. Chambers, Z. Liu, M. R. Freeman, and F. A. Hegmann, "Emission and detection of terahertz pulses from a metal-tip antenna," J. Opt. Soc. Am. B **22**, 2357–2365 (2005).

[22] B. S.-Y. Ung, J. Li, H. Lin, B. M. Fischer, W. Withayachumnakul, and D. Abbott, "Dual-mode terahertz time-domain spectroscopy system," IEEE Trans. Terahertz Sci. Technol. **3**, 216–220 (2013).

[23] G. Cataldo, J. A. Beall, H. Cho, B. McAndrew, M. D. Niemack, and E. J. Wollack, "Infrared dielectric properties of low-stress silicon nitride," Opt. Lett. **37**, 4200 (2012).

[24] H. T. Chen, "Interference theory of metamaterial perfect absorbers," Opt. Express **20**, 7165–7172 (2012).

[25] G. Duan, J. Schalch, X. Zhao, J. Zhang, R. D. Averitt, and X. Zhang, "Identifying the perfect absorption of metamaterial absorbers," Phys. Rev. B **97**, 035128 (2018).